Since January 2020 Elsevier has created a COVID-19 resource centre with free information in English and Mandarin on the novel coronavirus COVID-19. The COVID-19 resource centre is hosted on Elsevier Connect, the company's public news and information website.

Building and Environment 137 (2018) 185–197

Contents lists available at ScienceDirect

Building and Environment

journal homepage: www.elsevier.com/locate/buildenv

CFD investigation on the effects of wind and thermal wall-flow on pollutant transmission in a high-rise building

Di Mu, Naiping Gao*, Tong Zhu

School of Mechanical Engineering, Tongji University, Shanghai, China

ARTICLE INFO

Keywords:
Wind effect
Thermal plume
High-rise building
Pollutant transmission
Simulation

ABSTRACT

The solar radiation can heat the building outer surface, and then cause the upward natural convection flows adjacent to the wall. This phenomenon is especially obvious on a windless sunny day. The near wall thermal plume can drive gaseous pollutants released from lower floors to upper floors. Combined with the effect of ambient approaching wind, the transmission routes will be very complicated. The paper aims to investigate the airflow patterns and pollutant transmission within a building under the effects of wind and thermal forces. A hypothetical twenty-storey slab-shape high-rise building in Shanghai with single-sided natural ventilation is set as the research object in the present study. The intensity of solar radiation on a typical day during transition season is theoretically analysed. The temperature difference between the heated building envelope and the ambient air is calculated by a simplified heat balance model. Finally, the tracer gas method is employed in the numerical simulation to analyse the influence of the wind and wall thermal plume flow on the inter-flat pollutant transmission characteristics. The results show that, the temperature difference between sunward and shady side wall is about 10 K at noon on the designate day. When the source is set as a point with steady intensity and the buoyancy is stronger than or approximately equivalent to the wind, the reentry ratio of the flat immediately above the source can be around 25%.

1. Introduction

The environmental and public health issues are quite important concerns worldwide. Understanding how contaminants continue to pose a significant threat to human health is highly emphasized. The airflow can carry hazardous air pollutants moving within a room or between rooms even buildings to influence the residents' health [1]. Such long-distance routes of transmission are called airborne transmission, which is reported to be one of the major respiratory syndrome transmission routes by numerous engineering and epidemiological studies [2–5]. A lot of researches involving airflow patterns and aerosol-transmitted scenarios in multiscale area have been done by on-site full-scale measurements, reduced-scale wind/water tunnel experiments and computational fluid dynamics (CFD) techniques [6–9]. For urban scale, the airflow is complicated because of the interaction with the inhomogeneous underlying surfaces [8]. For street scale or building arrays, the microclimate in the street canyon or a neighborhood area will influence the natural ventilation process of buildings. The pollutants from vicinity, like traffic exhaust, dust and atmospheric aerosols, can easily penetrate into the indoor environment [9–11]. For indoor circumstance, studies about the travel of airborne infectious pathogens in hospitals, schools, offices, homes, aircraft cabins and other indoor environment have been performed to illustrate the pollutant behavior and help to guide the air distribution design [10–13]. Li et al. [14] reviewed over 40 multidisciplinary studies and demonstrated the evidence of interconnection between building ventilation and the transmission of airborne infections.

Regarding the isolated building environment, a special transmission mode called vertical cross-floor contamination has been detected, the cooking fume from lower floor to upper one is a very telling example for such physical phenomena. The airborne fine droplets can be carried upwards by buoyancy-forced air convection flow [15]. Thus, the upward contaminant flow can take the potential health issues to the neighbor upstairs. This inter-flat infection path is firstly identified and explored after the Severe Acute Respiratory Syndromes (SARS) clusters occurred in several high-rise residential buildings in Hong Kong, where the most affected occupants dwelled along the same vertical blocks on different storeys [16–18]. Li et al. implemented a study for the largest SARS outbreak in Ward 8A at Prince of Wales Hospital [17] and in Block E of Amoy Garden [18]. They also verified the probability to reduce airborne infection by optimizing the ventilation performance in the hospital wards [19]. Pressure control methods have been

* Corresponding author.
E-mail address: gaonaiping@tongji.edu.cn (N. Gao).

https://doi.org/10.1016/j.buildenv.2018.03.051
Received 20 January 2018; Received in revised form 28 March 2018; Accepted 28 March 2018
Available online 01 April 2018

considered as an effective technology to control the transmission of infectious virus in hospital environment [20]. Nevertheless, such strategies are not feasible for those residential buildings without centralized ventilation systems. Therefore, the process of pollutant inter-flat transmission in residential buildings is generally elaborated in the light of the mechanisms of natural ventilation. As to the contaminants in residential buildings, the proliferation and accumulation of harmful components or odors such as second hand tobacco smoke and volatile organic compounds (VOCs) may also cause a health concern. Several studies revealed that the passive tracer gas method can be used for reflecting the movement and distribution of gaseous pollutants or fine particles [21,22].

Based on the above facts and work, Niu et al. [23] first proposed a possible airborne re-entry behavior of inter-flat cross-contamination driven by indoor/outdoor temperature difference under the condition of single-sided natural ventilation through open windows. Previous on-site tracer gas tests and numerical simulations on buoyancy-forced inter-flat dispersion well explained and quantified the vertically upward transport of gaseous pollutants [24,25]. Subsequently, a series of wind tunnel tests [26–30] and numerical calculations [31–33] were carefully carried out to explore the inter-flat transmission dominated by wind force. Mao et al. [34] reviewed the mechanisms and evaluation indexes for the airborne transmission and dispersion between flats by single-sided natural ventilation in high-rise residential buildings. In general, it has been revealed from the previous studies that in the single-sided ventilation mode, the airflow exchange and migration of contaminants within the building are normally driven by wind effect, buoyancy effect, or combined wind and buoyancy effect. The synoptic wind speed and direction have an essential impact on the strength of wind effect [35,36]. For the buoyancy effect, one inducement is the difference between indoor and outdoor temperature, the other one can be the thermal plume along the high-temperature walls heated by the solar radiation during the daytime, especially in windless or breezy sunny day [37]. Fan et al. [38] measured boundary layer structure along the sunward surface of a sixteen-storey building in Guangzhou, and concluded that the maximum velocity in the boundary layer at a height of 50 m is about 1.0–1.5 m/s with absent wind and a wall/air temperature difference of 14–20 K. Such strong thermal flow should not be neglected since the most common wind speed in the urban environment is in the range of 1.0–2.0 m/s [39]. Hence the buoyancy forces basically generated by solar radiation will be a particular consideration in this paper. Over the past dozen years, several literature published about the combined wind and thermal flow patterns in urban region. Xie et al. [40] calculated a set of CFD simulation cases to investigate the impact of solar radiation on pollutant dispersion in different street layouts and estimated the relative strength of thermally/mechanically induced flow using the ratio of Gr/Re^2. It was found that solar calefaction of a windward surface in a street canyon would give rise to an increase in pollutant concentration of the canyon. Richards et al. [41] performed wind tunnel measurements to simulate the thermal effects within the vicinity of a onefold building with leeward facade heating with the same parameter Gr/Re^2. They concluded that compared with the isothermal condition, the leeward recirculation lengths were shorter for both cases of $Gr/Re^2 = 0.9$ and 1.6 (non-isothermal conditions). The velocity field and temperature distribution within the recirculation area were obviously different between two non-isothermal cases. Larsen and Heiselberg [42] carried out a group of wind tunnel tests to create a scene of single-sided natural ventilation driven by wind pressure and temperature difference. They gave the velocity profiles and air-change rates in the openings, which greatly varied from wind force dominating to buoyant force governing. Bangalee et al. [43] set four different open window modes to investigate the flow structures of fluid-driven natural cross-ventilation. They found that a larger volumetric flow rate did not always ensure better replacement of the indoor air, and vice versa. Dama and Angeli [44] designed three cases on the wind and buoyancy induced natural ventilation in double skin facades and compared two flow patterns derived from a simplified building simulation model and CFD. Their results showed that CFD analysis can provide a deeper insight on surface-level heat transfer. Most of the studies mainly paid attention to the heat and mass transfer around a single building block or building arrays, but there is a lack of research work on the cross-contamination mechanism through outer window flush driven by the combined buoyancy and wind effect.

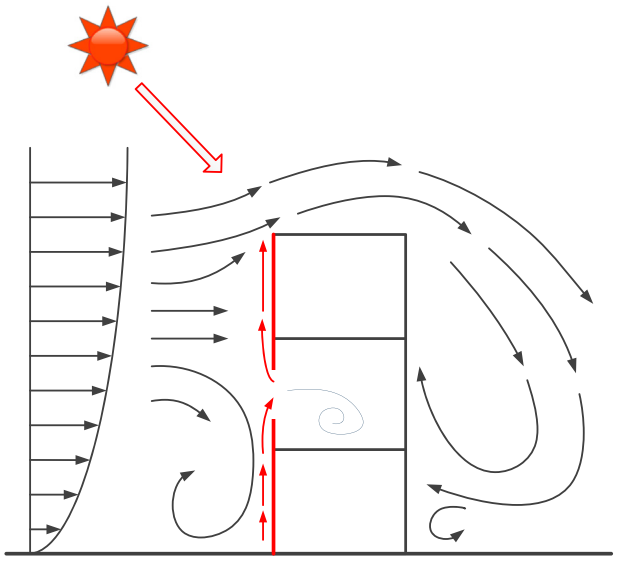

Fig. 1. Airflow directions around a rectangular building.

According to the wind-driven airflow around a bluff body under normal wind direction [45], there is a stagnation zone formed at the 2/3 height of the building on the windward side. The airflow above the stagnation zone goes toward the building top, while the airflow below the stagnation zone goes downward to the ground. The wall thermal plume can drive the gaseous pollutants released from lower unit to go to upper ones, especially in high-rise buildings. When the heated wall is on the windward side, the near wall airflow direction will change with the variation of the relative force of buoyancy and wind, notably in the approaching wind downward flow region in front of the building (Fig. 1). If the buoyant force is stronger, the flow patterns at the window opening should be inflows at the lower part and outflows at the upper part. When the wind force is stronger, the flow direction at the window opening can be downward. The purpose of the present work is to quantitatively explore the aforementioned phenomenon, namely the airflow field and pollutant transmission under effects of wind and thermal forces. A hypothetical twenty-storey high-rise building with single-sided ventilation is modelled as the research object. To quantitatively clarify the effect of solar radiation on the exterior wall surface of the building, the intensity of solar radiation on a certain day is calculated. Since the single-sided natural ventilation is usually used in transition season, we select a typical day from transition season as representative. Then the temperature difference between the heated wall and the ambient air is calculated using a simplified energy balance model of the building envelop. Finally, to analyse the influence of the wind and wall thermal plume flow on the pollutant transmission characteristics, the tracer gas method is employed in the numerical simulation. The results of present work are helpful for a profound understanding of how solar radiation and near-wall flow affect the vertical inter-flat contaminant transmission routes, and the results also reveal the combined effect of wind force and buoyancy lift on the pollutant dispersion near the building.

Table 1
Solar radiation intensity (W/m^2) in a typical day of transition season in Shanghai.

	11:00	12:00	13:00
Horizontal	888	923	886
Sunward	414	435	412
Shady side	164	168	164

Note: The atmospheric transparency is 0.62 [47–49]. During 11:00 to 13:00, the south face is sunward, while the north face is shady side.

2. Methodology

2.1. Temperature of wall surface

To quantify the strength of the natural convection adjacent to the wall, the temperature difference between the building surface and the ambient air should be clarified. The solar radiation intensity has a strong influence on the wall heating process, which needs to be quantified first. The wall temperature can be obtained by the heat balance calculation afterwards. The parameters of meteorology and building envelope refer to those of Shanghai, a city of hot/humid climate zone in China.

Based on the method given by Yan and Zhao [46], the solar radiation intensity (W/m^2) in the selected typical day on the horizontal plane and two vertical surfaces are calculated. The atmospheric transparency is set as 0.62 [47–49]. The results are shown in Table 1. During 11:00 to 13:00, the solar radiation intensity on the sunward side is in a small range of 410–440 W/m^2, while that of the opposite side is about 165 W/m^2. For both the sunward and shady side vertical walls at noon, the received solar radiation intensity changes in a very small range, which can be seen as a steady-state condition for the following calculation.

The temperature of outer wall surface increases after receiving the solar radiation. There is heat conduction between outer and inner wall surfaces, heat convection and radiation heat exchange with the ambient environment (Fig. 2). Because of the wall thermal inertia, the external wall will not reach the highest temperature when the solar radiation is the strongest, as well as the internal wall. In the present study, the time-average states are concerned. So the thermal lag on the temperatures of wall surfaces and indoor air is neglected in the theoretical calculation.

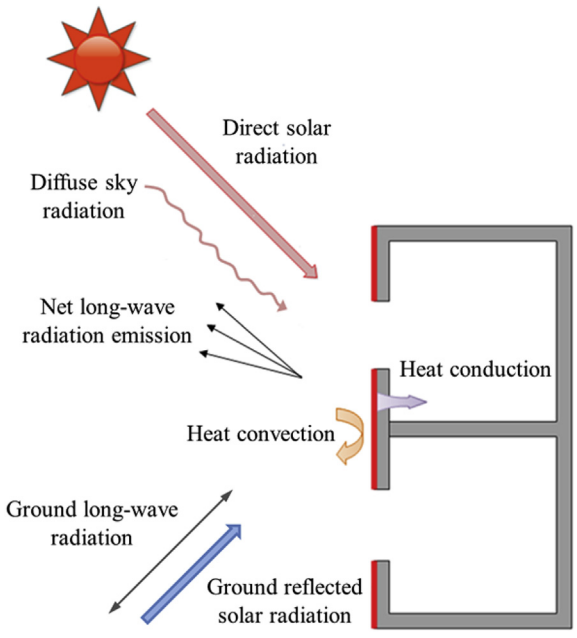

Fig. 2. Schematic of outer wall heat balance.

For an isolated building in a relatively open terrain, suppose the temperature distribution on the outer wall surface is uniform, which means no vertical and horizontal temperature difference. The steady-state heat balance can be described as Eq. (1),

$$Q_{solar} = Q_{conduc} + Q_{convec} + Q_{lw} \tag{1}$$

Q_{solar} represents the solar radiation absorbed by the outer wall surface, W/m^2, the equation is as Eq. (2),

$$Q_{solar} = \alpha_w I_{SV} \tag{2}$$

where α_w is the wall absorption. I_{SV} is the received solar radiation by vertical outer wall, which includes the direction solar radiation, diffuse sky radiation and ground reflected solar radiation.

Q_{conduc} represents the heat conduction from the outer wall surface to inner, W/m^2, the equation is as Eq. (3),

$$Q_{conduc} = \frac{T_{wout} - T_{win}}{\frac{\delta_w}{\lambda}} \tag{3}$$

where T_{wout} is the temperature of outer wall and T_{win} means the temperature of inner wall. δ_w represents the wall thickness and λ is the thermal conductivity. δ_w/λ is the thermal-conduction resistance, set as 1.1 m^2 K/W [50].

Q_{convec} is the heat convection exchange between the outer wall surface and the ambience, W/m^2, see Eq. (4),

$$Q_{convec} = h_{out}(T_{wout} - T_{aout}) \tag{4}$$

where T_{aout} is the ambient air temperature, h_{out} represents the convective heat transfer coefficient, W/(m^2·K). According to Ref. [50–52], the value of h_{out} can be calculated by Eq. (5),

$$h_{out} = 18.63U_w^{0.605} \tag{5}$$

When the coming wind is below 2 m/s, the wind speed near the windward wall U_w has a reference value of 0.5 m/s [53], so h_{out} = 12.2 W/(m^2·K).

Q_{lw} is the longwave radiation heat exchange between the outer wall surface and the surroundings, W/m^2, here only the atmospheric longwave radiation to the sky is considered, see Eq. (6),

$$Q_{lw} = \sigma\varepsilon_w x_{sky}(T_{wout}^4 - T_{sky}^4) \tag{6}$$

where σ is the Stephen Boltzmann constant, 5.67 × 10^{-8} W/(m^2·K^4). ε_w represents the system emissive of the outer wall surface longwave radiation, which is 0.9. x_{sky} is the angle factor between the vertical wall and the sky, which is 0.5. T_{sky} is the sky effective temperature, see Eq. (7) [54],

$$T_{sky} = 0.0552T_{aout}^{1.5} \tag{7}$$

For the inner wall surface, suppose the temperature difference between surfaces is small, then the radiation heat transfer can be neglected. The heat balance equation is as following Eq. (8),

$$Q_{conducin} = Q_{convecin} = h_{in}(T_{win} - T_{ain}) \tag{8}$$

$Q_{conducin}$ represents the heat conduction received by the inner surface, W/m^2, the value is equal to Q_{conduc}. $Q_{convecin}$ is the heat convection exchange between the inner wall surface and the indoor air, W/m^2. The convective heat transfer coefficient h_{in} is set as 5 W/(m^2·K) [50]. Since a change of 1 K for the indoor air temperature T_{ain} only causes a 0.06 K variation of T_{wout}, the value of T_{ain} has a very small influence on the result of T_{wout}. The given value of T_{ain} is 3 K higher than T_{aout} in the calculation.

Based on the above equations and variable values, the temperature values of vertical sunward and shady side outer wall surfaces at noon can be calculated. The results are shown in Table 2. The solar radiation intensity is an average value of 11:00–13:00. It is observed that the temperature of the sunward outer surface is 10 K higher than the shady side, and 13 K higher than the outdoor air temperature. The calculation results are compared with the experimental data from Wang et al. [55].

Table 2
Parameters for outer wall temperature calculation.

Parameters		Value
Time		Noon
Outdoor air temperature (K)		288.15
Sky effective temperature (K)		270
Solar radiation intensity (W/m^2)	Sunward	420
	Shady side	165
Wall surface temperature (K)	Sunward	301.16
	Shady side	291.67

They selected a 40 m height rectangular student dormitory as the target building and measured several parameters including external wall temperature, wind speed, solar intensity and air temperature in April 7th and 16th in 2010. During their test process, the solar radiation received by the south wall at 11:00–13:00 was in the range of 300–350 W/m^2, the wind speed was below 4 m/s and the ambient temperature was 285–288 K. The temperature on the sunward surface varied with height. The largest difference between bottom and top was 2.5 K. The measured average temperature difference between the external south wall and ambient at 11:00–13:00 was 12–18 K. The calculation result in the present work is relatively small compared with the aforementioned measurements. In view of the other influence factors such as the wall thermal conductivity and radiation heat transfer, a 13 K temperature difference can be considered as a reasonable value. In the following numerical simulation, considering the computation accuracy for airflow on the windward side and the mesh quantity, the heated sunward and shady side walls are placed at the windward side in different cases separately. That is, in some cases the windward wall is sunward and in some cases it is shady side.

2.2. Physical model and case configuration

The CFD method is adopted by using a commercial program, Fluent 17.0. The building model and computational domain are shown in Fig. 3. A hypothetical twenty-storey high-rise building is set as the research object. The whole building dimensions are 58 m height(y), 18 m length(z), 9 m width(x). Thus the building model is a slab one with the length-width ratio of 2. Six rooms in this building are focused on, which fall into three groups and each group contains two neighboring units, respectively the 2nd, 3rd, 10th, 11th, 18th and 19th floors along the middle column of the building windward facade, which are located at the lower, middle and upper positon of the building separately. The dimensions of the concerned rooms are 2.9 m height(y), 3 m length(z), 3.6 m width(x). The window dimensions of each room are height (y) × width(z) = 1.5 m × 0.9 m. The bottom of the window frame is 0.9 m above the room floor. The dimensions of each room and window

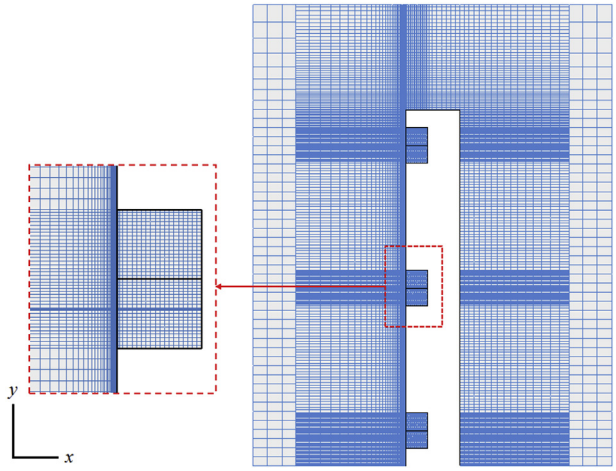

Fig. 4. Mesh system.

are in accordance with our previous wind tunnel tests [29,30]. The computational domain for the concerned cases is a rectangular zone surrounding the objective building. The domain size is carefully designed, considering both efficiency and accuracy. According to Franke et al. [56], the blockage ratio of the domain should be below 3%, which is about 1.8% in the present study.

As for the boundary condition, the windward surface is set as a heated wall with constant temperature listed in Table 2. The other walls of the building are assigned with adiabatic surfaces. Three different mesh systems of 3.5, 5.1, and 6.8 million grids are created and compared. The mesh refinement multiple is over 1.1 [57]. The medium one is selected because the latter two mesh systems generate similar values for air velocity and temperature at several specific locations in the computational domain. The near wall mesh on windward side is refined and $y^+ < 5$, as shown in Fig. 4. For the other surfaces, the value of y^+ is satisfied with $30 < y^+ < 300$. . The wind profile at the inlet of the computational domain is determined by the following power law Eq. (9) [58],

$$\frac{U(y)}{U_{ref}} = \left(\frac{y}{H}\right)^{0.22} \tag{9}$$

where H is the building height and U_{ref} is the reference wind speed at the building height. The turbulence on the inlet boundary is characterized by turbulence intensity and length scale, which are 10% and 1 m [25,59], respectively. The turbulent effect is simulated by the renormalization group (RNG) k-ε model [60] with enhanced wall treatment. The pressure-velocity coupling algorithm is SIMPLE. The pressure interpolation method is a staggered scheme named PRESTO. The

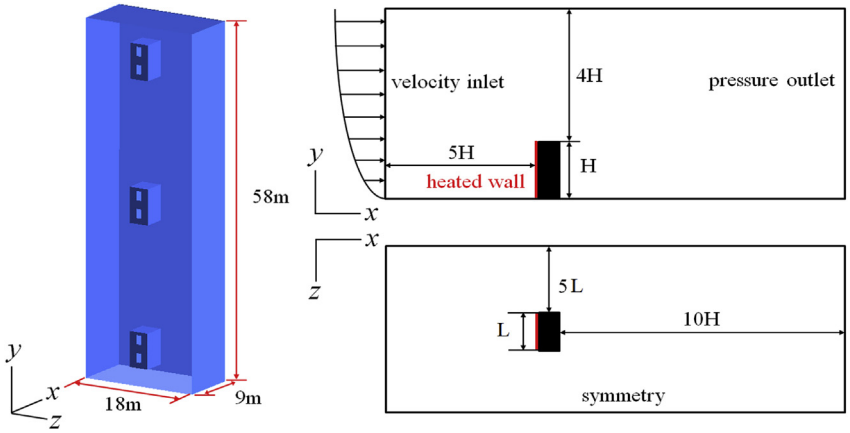

Fig. 3. Building model and computational domain.

Table 3
Configuration of numerical simulation cases.

Mode	Case No.	Case Name	U_{ref} (m/s)	$\triangle T$ (K)	*Re*	*Gr*	*Ri*
Close window	I1	C-Δ*T*13-*U*0.4	0.4	13	1.57×10^6	3.86×10^{14}	156.9
	I2	C-Δ*T*13-*U*0.6	0.6		2.35×10^6		69.7
	I3	C-Δ*T*13-*U*0.8	0.8		3.14×10^6		39.2
	I4	C-Δ*T*13-*U*1.0	1.0		3.92×10^6		25.1
	I5	C-Δ*T*13-*U*1.2	1.2		4.71×10^6		17.4
	I6	C-Δ*T*13-*U*1.6	1.6		6.27×10^6		9.8
	I7	C-Δ*T*13-*U*3.2	3.2		1.25×10^7		2.5
	I8	C-Δ*T*13-*U*6.4	6.4		2.51×10^7		0.6
Open window	II1	O-Δ*T*13-*U*0.4	0.4	13	1.57×10^6	3.86×10^{14}	156.9
	II2	O-Δ*T*13-*U*0.6	0.6		2.35×10^6		69.7
	II3	O-Δ*T*13-*U*0.8	0.8		3.14×10^6		39.2
	II4	O-Δ*T*13-*U*1.0	1.0		3.92×10^6		25.1
	II5	O-Δ*T*13-*U*1.2	1.2		4.71×10^6		17.4
	II6	O-Δ*T*13-*U*1.6	1.6		6.27×10^6		9.8
	II7	O-Δ*T*13-*U*3.2	3.2		1.25×10^7		2.5
	II8	O-Δ*T*13-*U*6.4	6.4		2.51×10^7		0.6
Open window	III1	O-Δ*T*3.5-*U*0.4	0.4	3.5	1.57×10^6	1.06×10^{14}	42.9
	III2	O-Δ*T*3.5-*U*0.5	0.5		1.76×10^6		27.5
	III3	O-Δ*T*3.5-*U*0.6	0.6		2.35×10^6		19.1
	III4	O-Δ*T*3.5-*U*0.8	0.8		3.14×10^6		10.7
	III5	O-Δ*T*3.5-*U*1.0	1.0		3.92×10^6		6.9
	III6	O-Δ*T*3.5-*U*1.6	1.6		6.27×10^6		2.7
	III7	O-Δ*T*3.5-*U*3.2	3.2		1.25×10^7		0.7
	III8	O-Δ*T*3.5-*U*6.4	6.4		2.51×10^7		0.2
Open window	Ref1	O-*U*1.0	1.0	isothermal	3.92×10^6	–	0
	Ref2	O-*U*3.2	3.2	isothermal	1.25×10^7	–	0

discretization scheme used for the other variables except the pressure is second order upwind to ensure the computational precision. As to the pollutant transmission, a 1×10^{-6} m^3 tiny cube at the middle of the window is assigned as the source, located at the 2nd, 10th and 18th floor respectively in each case. Propane (C_3H_8) [26–28], as a tracer gas of gaseous pollutants, is generated at a constant mass flow rate of 8 mg/s [25,31]. It takes more than 10000 iterations for every simulation to reach the convergence. The calculations are terminated when the residuals do not show any further reduction and maintain at a reasonable level. The convergent values of residuals are as following: 10^{-4} for continuity, 10^{-5} for *k*, *ε*, *x*-, *y*- and *z*-velocity, 10^{-6} for concentration and 10^{-8} for energy. The solutions, such as the air velocity, temperature and concentration at specific points, are stable or appear steady quasi-periodic variations with acceptable fluctuation amplitudes. The amplitudes of velocity and concentration values at specific points show significant ones in the buoyancy driven windless case, which are all below 8%.

Considering the effects of window active status, wind speed, temperature difference and source location, totally 78 cases are calculated. Table 3 shows 26 sets of configuration based on the airflow field without the influence of source, and these cases are divided into four groups according to the window condition and the temperature difference. “C” means close window mode and “O” means open window mode. A 13 K temperature difference represents that the building windward wall faces the sun, while a 3.5 K temperature difference means that the windward wall is the shady side.

A dimensionless number, Richardson number, is adopted to represent the relative strength of buoyancy lift and wind. The equation is as following Eq. (10),

$$Ri = \frac{Gr}{Re^2} = \frac{\beta \Delta T g H^3/\nu^2}{(U_{ref} H/\nu)^2} \tag{10}$$

where β is the thermal expansion coefficient, $((T_{aout} + T_{wout})/2)^{-1}$, K^{-1}, g is the gravity acceleration, 9.81 m/s^2 and ν is the kinetic viscosity, 1.48×10^{-5} m^2/s. *Gr* is the Grashof number reflecting the intensity of natural convection and *Re* is the Reynolds number characterizing the forced convention flow patterns. The building height is selected as the characteristic length since the flow direction along the windward heated wall is one of the biggest concerns. According to the parameters shown in Table 3, these cases contain the processes from natural convection to forced convection.

2.3. Model validation

The model involving pure wind driven inter-flat transmission has been validated in our previous paper [29]. Since the formation of airflow field around the present objected building is contributed to the combined effect of approaching wind and buoyancy, the mechanism contains the natural convection and wind driven airflow around a bluff body. The following two correlative cases are done to validate the accuracy of the numerical configuration.

2.3.1. Natural convection in a cavity

Betts and Bokhar [61] carried out a series of experiments to investigate the natural convection of air in a tall cavity. A portion of results are selected to certify the applicability of the numerical methods to predict the natural convection flow adjacent to the wall. The experimental cavity was 2.18 m height (*y*), 0.076 m width (*x*) and 0.52 m depth (*z*), with a cold wall of 15.1 °C and a hot wall of 34.7 °C (Fig. 5). Thus the temperature difference between these two vertical walls was 19.6 °C, corresponding to a Rayleigh number of 8.6×10^5. A K-type thermocouple was used for measuring the temperature distribution in the cavity and the accuracy was about 0.1 °C. The velocity field was measured by a laser doppler anemometry (LDA) system. In the simulation configuration, the RNG *k*-*ε* model including low-Reynolds number effect is employed to solve the flow pattern. The enhanced wall treatment combining a two-layer model is used for improving the prediction of the boundary layer flow and the heat transfer in the near wall area. As shown in Fig. 5, the wall-adjacent grids are refined with y^+ below 5.

The profiles in Fig. 6 illustrate the comparisons of the temperature and velocity distribution results between the experiment and simulation at three different heights of the central *x*-*y* plane. It can be seen that the temperature rises up from the cold wall to the hot wall. The temperature profiles have two changes of gradient along the width direction, and the variation of temperature on each gradient is not exactly linear.

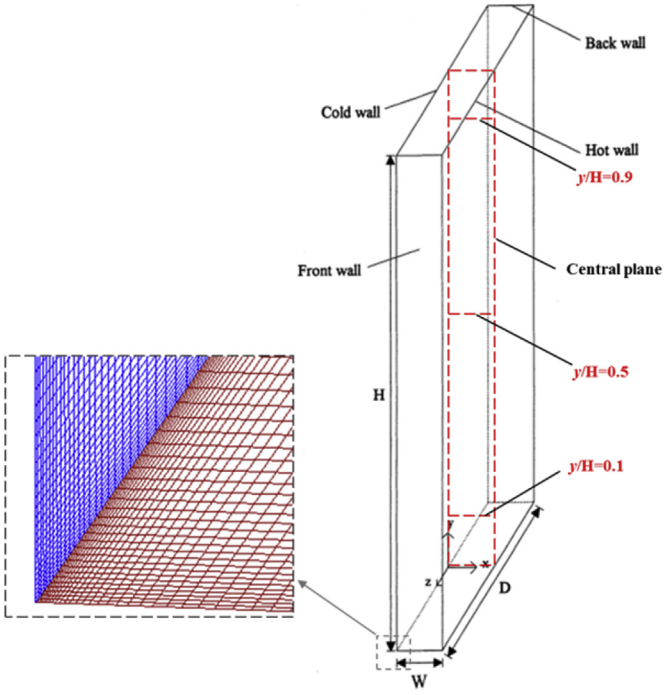

Fig. 5. A schematic view of the air cavity with natural convection.

For the velocity profiles, the positive values mean the airflow direction is upward, while the negative ones mean downward. Thus the airflow moves upward near the hot wall and downward near the cold wall. The velocity magnitude near the walls is relatively larger than that at the central section of the cavity except the confined wall-adjacent regions where the airflow is adhered by the walls. There are some tendencies in common between the corresponding temperature and velocity lines. The first thing is that the gradient near walls is relatively higher than that at the central part. The next one is that at the upper height ($y/H = 0.9$), the gradient near the hot wall is lower than that near the cold wall, and the simulation results at the middle part are slightly smaller than those at the near wall part. Whereas at the lower height ($y/H = 0.1$), the gradient near the hot wall is larger, and the simulation results at the middle part are mildly higher than at the near wall part. Another one is that high quality of anti-symmetry shows in the mid-height test line ($y/H = 0.5$) across the cavity. In general, although there are deviations between simulation and experimental results, the coincidence rate is acceptable enough.

2.3.2. Air flow around a bluff body

Jiang et al. [62] performed several sets of wind tunnel tests to measure the airflow patterns around a building-like cubic model with the dimensions of 250 mm height (y) × 250 mm length (x) × 250 mm width (z), and the wall thickness of 6 mm. The model had an opening on the windward side wall and the size was 125 mm (y) × 84 mm (z), resulting in wind-induced single-sided ventilation. The mean and fluctuating velocity distributions along 10 vertical lines at the middle x-y plane, ranging from 25 to 500 mm in height, were measured by a one-dimensional LDA with a resolution of ± 0.05 m/s. The mean velocity

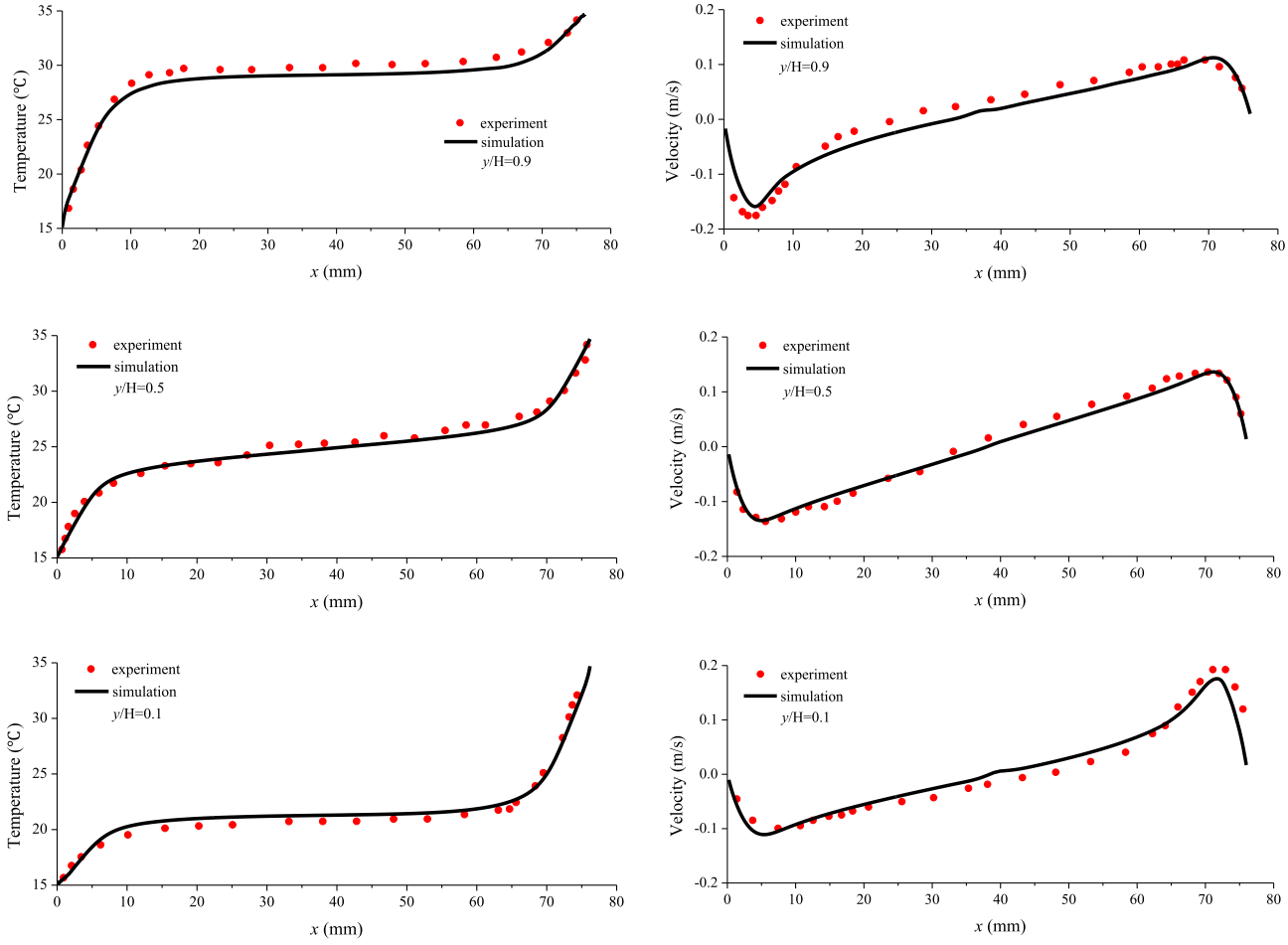

Fig. 6. Comparisons of temperature and velocity profiles between simulation and experiment at different heights of the central x-y plane.

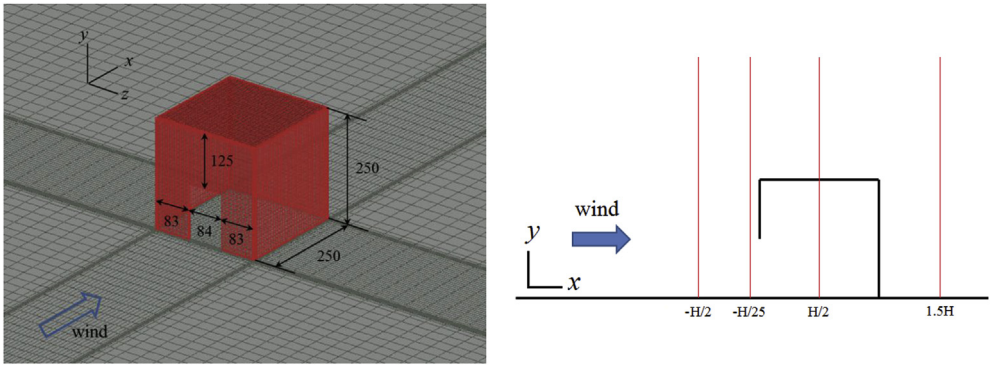

Fig. 7. Sketch of the cubic model and the locations of velocity test lines.

distributions along four of these test lines are picked for the validation of the simulation results (see Fig. 7). In the numerical simulation, the computational domain had a height of 5*H*, an upstream length of 5*H*, a downstream length of 10*H*, and a lateral length of 5 L on both sides. The inflow velocity profile in the *x*-direction followed a logarithmic law, $U(y) = (U_{ref}/\kappa)\ln(y/y_{ref})$, where κ is the Von Karman constant, 0.41, and y_{ref} has a value of 0.005 m. The velocity components in the other two directions are zero. The turbulence on the inlet boundary is given by turbulence intensity and length scale, which are 10% and 0.25 m, respectively. The structured hexahedral mesh elements are adopted to construct the whole computational domain. The grids on the ground and cubic model surfaces are also shown in Fig. 7. The near wall meshes of the building model are locally densified with the minimum grid width of 0.1 mm. The RNG *k-ε* model combined with enhanced wall treatment is used again for reproducing the airflow field feature.

Fig. 8 shows the streamlines at the middle *x-y* section obtained by numerical simulation. The comparisons of four velocity profiles at the middle *x-y* section between simulation and experiment are shown in Fig. 9. The positive value of U/U_{ref} means the airflow direction is the plus *x* direction, and the negative one means the airflow move to the minus *x* direction. It can be seen that the backflow vortex at the bottom before the cubic model in Fig. 9(a) (line -*H*/2) and Fig. 9(b) (line -*H*/25), the reverse flow on the roof in Fig. 9(c) (line *H*/2) and the recirculation zone in the downstream region in Fig. 9(d) (line 1.5*H*) are captured by the present simulation. The simulated velocity distributions are satisfactory compared with the measurement except along the line 1.5*H* behind the model. The minus simulated velocities at the lower section of the line 1.5*H* mean that RNG *k-ε* model predicts a mildly larger separation region in the wake flow of a bluff body. Despite the slight inaccuracy of RNG *k-ε* model in the prediction of the vortex-shedding effects in the building wake, the calculations of the airflow field inside the cubic model and in the upstream areas near and beside to the windward façade agree well with the experimental results. It is sufficient to justify the application of RNG *k-ε* model in the present main concern of inter-flat pollutant transmission on the windward side and the qualitative pollutant distribution behind the building.

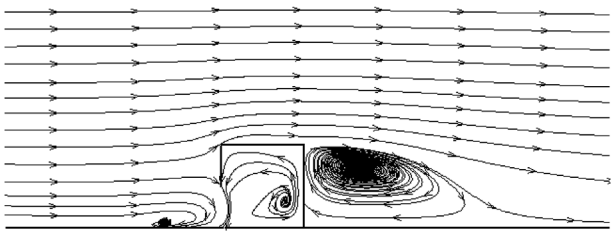

Fig. 8. Streamlines at the middle x-y section.

3. Results and discussion

The work in this section contains two parts. For the isolated building scale, concerning the comprehensive performance of combined wind and buoyancy effect, part 3.1 gives the airflow streamlines and tracer gas mass fraction distribution around the building in the close window mode. Since the heated wall is on the windward side, the thermal plume generated by natural ventilation is adjacent to the windward surface. Part 3.2 firstly shows the concentration distribution along the windward wall in the open window mode. Then for the room scale, part 3.2 illustrates the mean temperature and air exchange rate (ACH) of each room. Furthermore, an evaluation index, reentry ratio, is introduced in to analyse the inter-flat transmission characteristics. So this part mainly concerns the situations within the objective building.

3.1. Airflow and tracer gas concentration distribution in close window mode

To compare the airflow patterns around the building in different cases, the velocity magnitude distribution on a portion of middle *x-y* plane for four representative close window mode cases are shown in Fig. 10. In Fig. 10(I1), *Ri* = 156.9, the buoyancy lift is dominant. The thermal plume along the windward surface can be observed distinctly and the flow over the building roof moves downstream toward the high sky. The wall thermal flow velocity at the building height is up to 1.2 m/s. The airflow near the leeward surface is upward. Since the thermal air from upstream flows to the upper space of downstream, the air density and pressure of the upper zone are smaller than those of the lower zone. That should be one of the main reasons for the upgrade airflow on the leeward side. In Fig. 10(I3), the coming wind speed at the building height is 0.8 m/s, the corresponding *Ri* is 39.2. It can be seen that the wall flow scope is weakened due to the suppression effect of the approaching wind. The airflow above the roof and behind the building is more likely to go to the downstream rather than to the higher altitude. A reverse vortex can be observed behind the building. In Fig. 10(I4), the corresponding *Ri* is 25.1. The airflow closely adhering to the windward wall still tends to go upward. The velocity magnitude near the windward wall is below 0.5 m/s. A small backflow vortex forms at the windward bottom area. As the approaching wind speed goes up, and the temperature difference is constant, a stagnation zone shows between 16th and 17th floor on the windward side, as shown in Fig. 10(I7). The downward flow below the stagnation zone has a velocity magnitude of about 1.0 m/s. The near wall upward thermal flow is severely restrained. The recirculation vortexes on the leeward side can be observed. Because of the relatively high wind speed, the airflow pattern in this case is almost the same with the pure wind driven airflow around a bluff body [45].

As to the pollutant dispersion characteristics, the tracer gas is released as a point source at a constant mass flow rate from one windward unit in each case. To observe the pollutant transmission routes and compare the concentration distributions, Fig. 11 gives the tracer gas

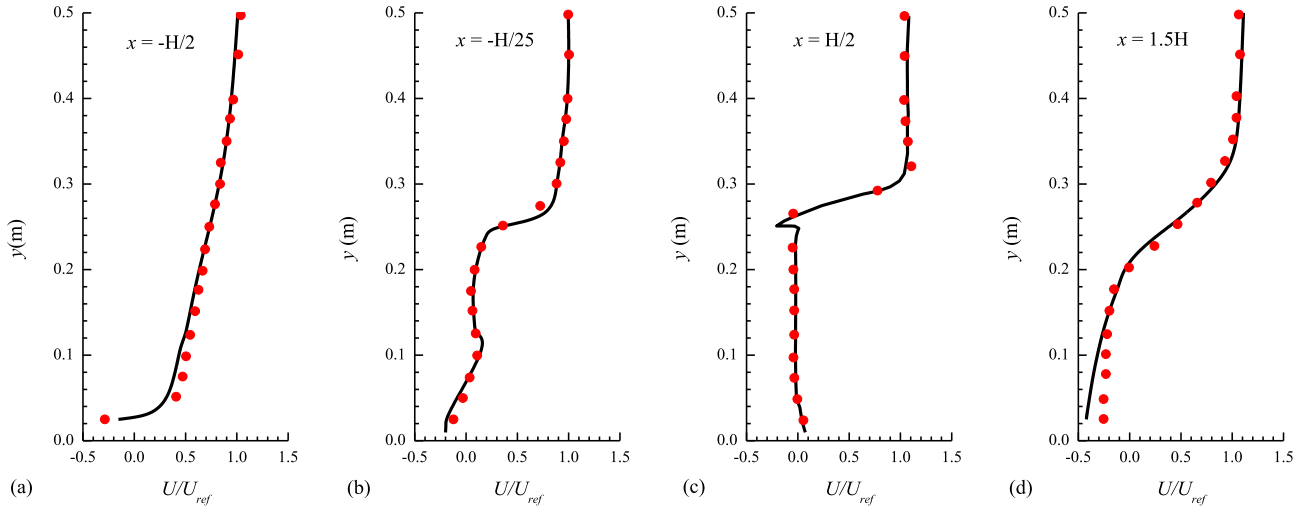

Fig. 9. Comparisons of the mean velocity along the test lines between simulation and experiment.
(● experiment; — simulation).

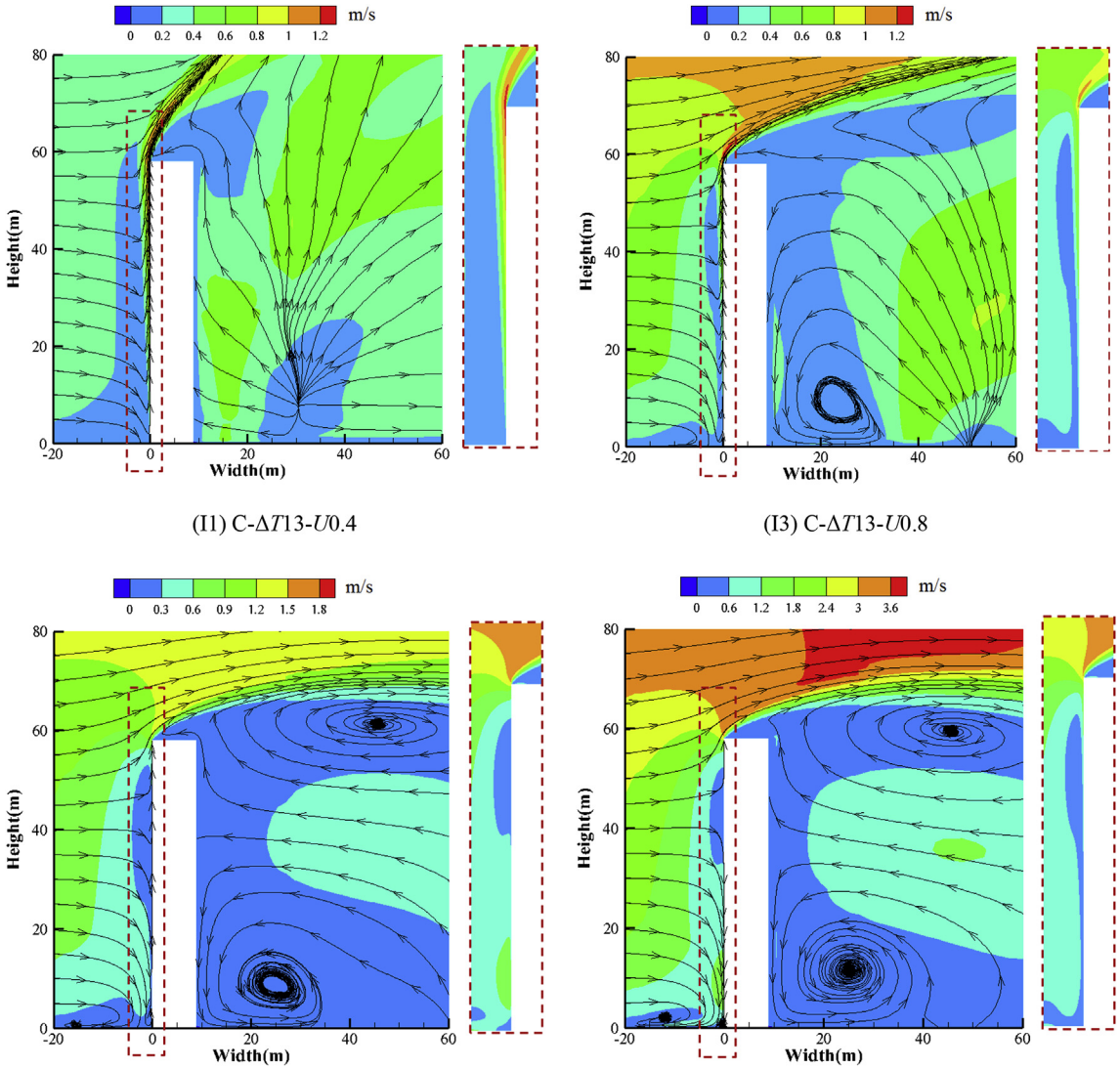

Fig. 10. Streamlines and velocity magnitude contours in the middle xy section.

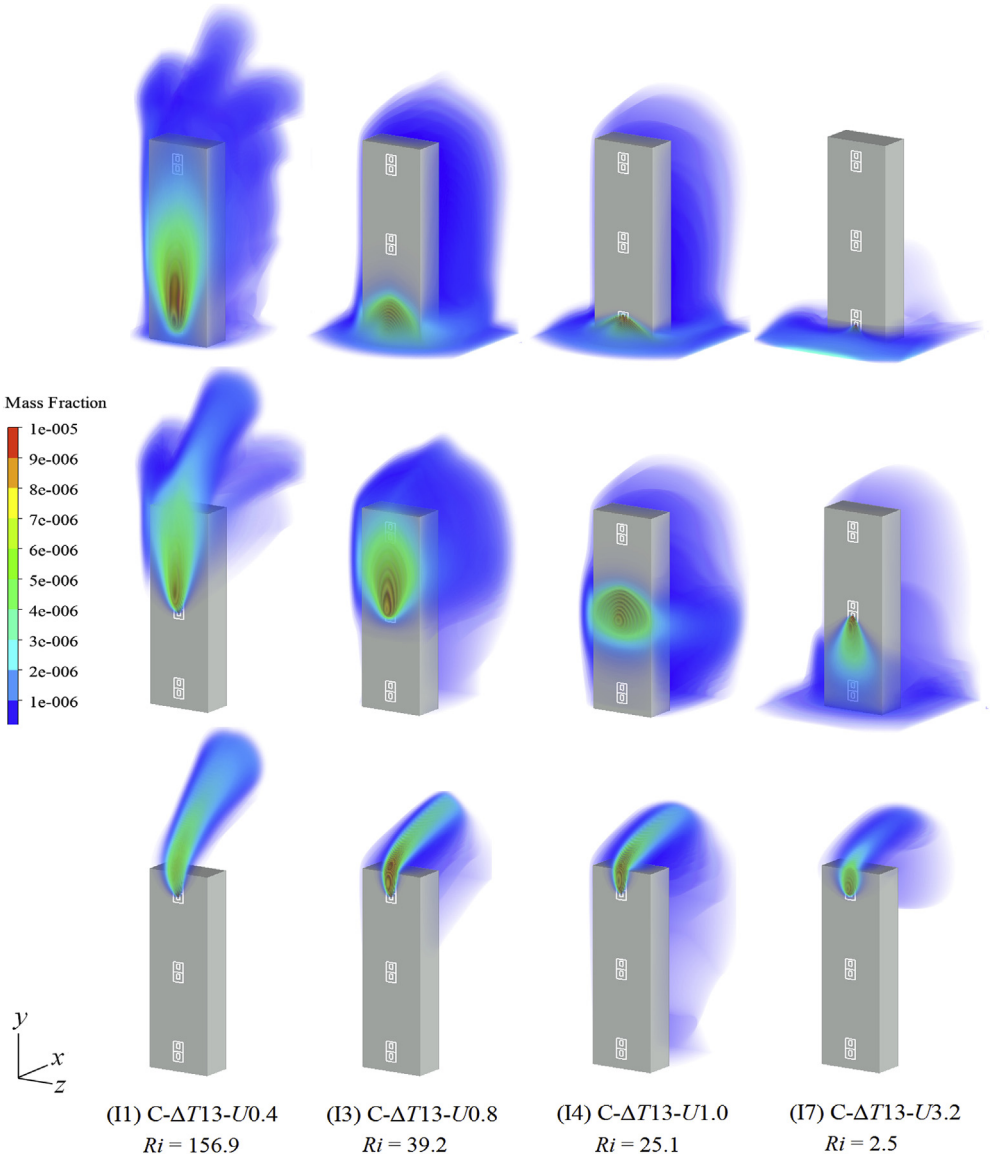

Fig. 11. Tracer gas concentration distribution around the building in close window mode.
(The source location is the 2nd floor in the upper row figure, 10th floor in the middle ones and 18th floor in the lower ones).

mass fraction distributions around the building in twelve typical cases separately. The illustrated results can be divided into three groups based on the different source locations. When the source is located at the windward 2nd floor, in Case I1, the shape of the concentration in the range of 10^{-6}-1 shows a symmetrical balloon form on the windward wall, and the vertical coverage area contains the 2nd floor to the 18th floor along the middle column of the building windward surface. In Case I3, the *Ri* number is reduced from 156.9 to 39.2, the infected area on the windward side reflects a peach-like shape around the source unit. Both the vertical and horizontal transmissions are limited. Part of tracer gas can be taken to the front of building because of the backflow at the windward bottom region, and then spread to the lateral side. In Case I4, the upward transmission on the windward side is totally suppressed by the downward coming wind, the tracer gas spread toward the ground and to the downstream with airflow, which means the buoyancy lift is weaker than the approaching wind at lower height. In Case I7, the infected area is mainly restricted at the bottom in front of the building, which is influenced by the bottom airflow vortex when the approaching wind is ruling. For the region behind the building, the concentration magnitude is mostly below 10^{-6}. In Case I1, although the thermal plume is dominant, the gentle wind still takes a part of tracer gas bypassing the lateral side to the leeward side during the upward transmission process along the windward surface. In Case I3 and Case I4, where the *Ri* number is 69.7 and 39.2 respectively, the affected phenomenon is relatively more obvious due to the horizontal dispersion from the windward side and the upward near wall airflow on the leeward side. When the *Ri* number decreases to a relatively low value of 2.5, in Case I7, the tracer gas mainly moves to the upstream with the bottom backflow and then to the lateral.

When the source location is at the windward 10th floor, the vertical coverage area of 10^{-6}-1 range along the windward wall is from the source floor to above the building top and still shows a symmetric shape in Case I1. Since the thermal flow speed is faster at the upper height of the building, the windward tracer gas is brought to high altitude quickly, so the leeward space is barely affected. In Case I3, the wind speed is higher than in Case I1, the effect of the near wall thermal flow is weakened. The tracer gas still goes up to the top of the building and the vertical coverage area is smaller than that in Case I1, while wider in horizontal direction. Part of tracer gas can cross the building roof moving to the downstream and the upper space on the leeward side is

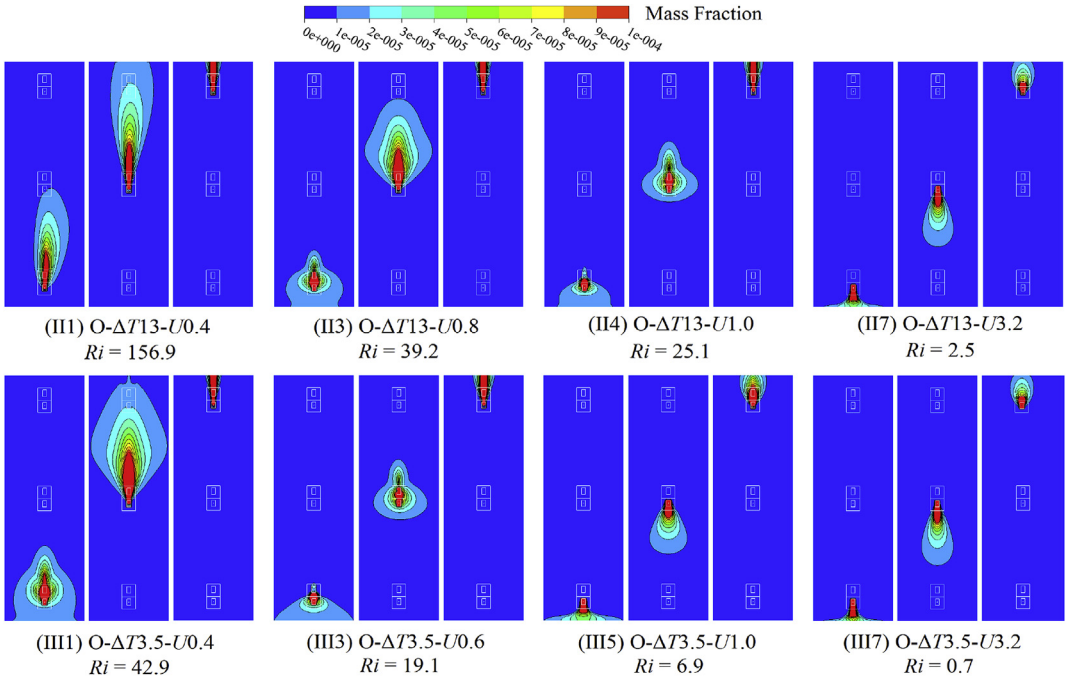

Fig. 12. Tracer gas concentration distribution on the windward wall in open window mode.

affected. In Case I4, due to the low velocity along the windward wall, the tracer gas tends to spread in a small region around the source on the windward side. The region behind the building also suffers. As the *Ri* number reduces to 2.5 in Case I7, the wind effect is dominant, the windward covered area seems like raindrop going downward because of the vertical downward airflow. The leeward space is affected, but slightly less than the former case.

When the source location is at the windward 18th floor, the tracer gas wouldn't disperse downward since the thermal plume and the airflow above the stagnation zone are both upward. The units on the leeward side are softly affected in Case I4. Overall, in the buoyancy lift governing cases (II-II3), the tracer gas mainly spreads from source unit to the upper ones on the windward side. In the two forces equivalent cases (II4), the tracer gas mainly disperses horizontally from windward side to leeward side. In the wind force ruling cases (II5-II8), the tracer gas mainly moves from the source unit to the lower ones on the windward side.

3.2. Tracer gas concentration distribution in open window mode

Fig. 12 illustrates the tracer gas mass fraction distributions along the windward wall in each case of group II and group III. The overall tendency of group II is similar with that of group I, the close window mode. In the windless case II1, the velocity of vertical upward flow adjacent to the wall increases with height. So compared with the source location at 2nd floor, the tracer gas releasing from the 10th floor moves upward faster and has a longer vertical coverage. When the source is located at the 18th floor, the tracer gas covers a wider range at the horizontal direction in Case II7 where the wind force is ruling than that in II1 under buoyancy lift dominated condition. In group III, the temperature difference is 3.5 K. Under the same breeze condition, the vertical upward transmission in Case III1 is weaker than Case II1 due to the smaller thermal plume. In Case III5 and III7, the *Ri* number is less than 7, the wind force is predominant. With the source releasing from the 10th floor, the shape of tracer gas coverage is like raindrop as mentioned above and the breadth of the raindrop decreases from Case III5 to III7, while the raindrop length increases. The reason is the growing downward airflow speed below the stagnation zone.

For each room in the objective building, open window mode means

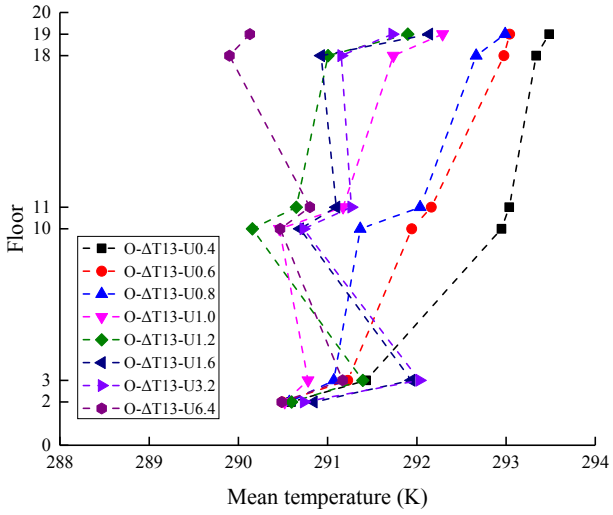

Fig. 13. Average indoor air temperature of each room.
(Open window mode, wall/ambient air temperature difference is 13 K).

single-sided natural ventilation. There's inside/outside heat transfer and air exchange through openings, resulting in inter-flat transmission. The mean indoor air temperature in each room of group II is shown in Fig. 13. Since the heat conduction from the building envelope is neglected in the simulation, the indoor air temperature can be slightly underestimated. One common thing can be observed from the profiles that for two neighbor flats, the mean indoor air temperature in the upper one is higher than that in the lower one. As for the differences, the profiles of eight cases can be divided into three classes according to the variation tendencies of 3rd → 10th and 11th → 18th. Class one contains three cases under the condition when the approaching wind speed is in the range of 0.4 m/s - 0.8 m/s and the buoyant lift dominates the near wall airflow. In this class, the mean indoor air temperature in the concerned room increases with height, which should contribute to a stronger thermal plume at a higher height. For a certain flat, the temperature level increases with *Ri* number. The reason is that a higher approaching wind can take away more heat by convection, so less heat

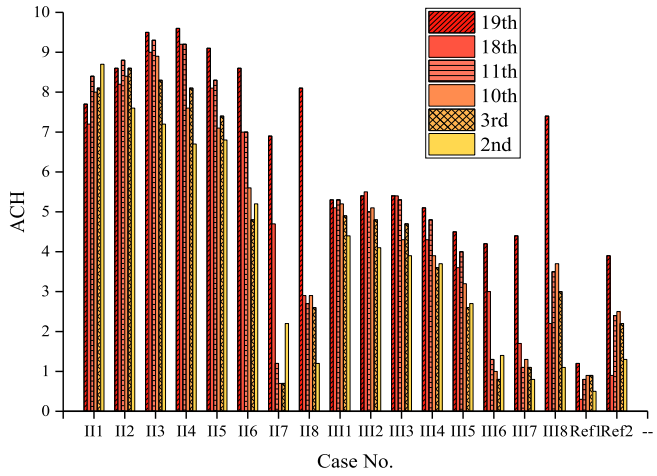

Fig. 14. Air exchange rate (ACH) of each room.

enters in the room, resulting in a relatively lower indoor temperature. Class two refers to cases with the wind speed of 1.0 m/s and 1.2 m/s. The slope from 3rd to 10th floor is negative, while from 11th to 18th floor is positive. The reason might be that the thermal flow is suppressed below the stagnation zone, whereas it still exists at the higher region. Class three contains three wind force dominated cases. The slopes of both 3rd → 10th and 11th → 18th are negative. Since the downward airflow is strong at the lower half part of the building height, the wall heat also transfers downward. In general, the indoor/ambient air temperature difference is in the range of 2 K−6 K.

The ACH (air exchange rate) is calculated by an integral method [62], see Eq. (11),

$$\mathrm{ACH} = \frac{0.5\int_0^A |U_x| dA}{\mathrm{Vol}} \tag{11}$$

where the U_x is the velocity normal to the window, m/s, A represents the window area, m^2 and Vol is the room volume, m^3. Since the airflow from outside is likely to form a small circuit at the opening window and the effective depth of fresh air is limited, the calculation result by this method is considered to be slightly higher than the tracer gas decay method, but the value is testified very close to the empirical models [25]. The ACH values of six concerned units in different cases are listed in Fig. 14. In general, the ACH values change in a big range of 0.5–10. When the *Ri* numbers are approximate, the ACH values in group II are mostly higher than those in group III. Take Case II4 (U_{ref} = 1.0 m/s, ΔT = 13 K, *Ri* = 25.1) and III2 (U_{ref} = 0.5 m/s, ΔT = 3.5 K, *Ri* = 27.5) as an example, the *Ri* numbers in these two cases are very close, while the ACH value in the former case is 1.5–2.0 times that of in the latter case for the same room. The reference coming wind speed in the former case is twice that of in the latter one. The temperature difference between the outer windward wall and the ambient in Case II4 is higher than in Case III2, so the thermal plume in Case II4 is stronger. These phenomena also appear in other corresponding conditions, such as Case II5 and Case III3, Case II6 and Case III4. This might be concluded that under the coupling effect of wind force and buoyancy lift, the relative magnitude of wind and thermal plume is quite crucial for ACH value of the room. Another thing can be found from Fig. 14 is that in the wind force predominant cases when *Ri* < 5 (II7, II8, III7, III8, Ref1, Ref2), the ACH values are lower than those in the buoyancy lift governing conditions or the two forces equivalent cases (II1-II4 and III1-III3), except for the 19th floor.

To evaluate the potential inter-flat pollutant transmission, the quantifying method proposed by Niu and Tung [23] is used for analyzing the possibility of reentry. The reentry ratio, *R*, is defined as the fraction of the exhaust air from a source unit *i* which reenters another unit *j*, which can be calculated by Eq. (13):

$$R = M_{i-j}\frac{\mathrm{Vol}_j(ACH)_j}{\mathrm{Vol}_i(ACH)_i} \tag{13}$$

$M_{i\text{-}j}$ represents the mass fraction of air that originates from the source room *i* and is present in another room *j*. In the present work, the pollutant concentration in a unit is represented by the mean

Reentry ratio (%) 100 1 0.01

Case No.	II1	II2	II3	II4	II5	II6	II7	II8	III1	III2	III3	III4	III5	III6	III7	III8	Ref1	Ref2
Ri	156.9	69.7	39.2	25.1	17.4	9.8	2.5	0.6	42.9	27.5	19.1	10.7	6.9	2.7	0.7	0.2	0	0
19th	0.11	0.01																
18th	0.12	0.01																
11th	0.85	0.13							0.04									
10th	1.05	0.18							0.06									
3rd	20.56	24.62	19.97	4.69					19.09	12.35	2.82							
2nd	■	■	■	■	■	■	■	■	■	■	■	■	■	■	■	■	■	■

Case No.	II1	II2	II3	II4	II5	II6	II7	II8	III1	III2	III3	III4	III5	III6	III7	III8	Ref1	Ref2
Ri	156.9	69.7	39.2	25.1	17.4	9.8	2.5	0.6	42.9	27.5	19.1	10.7	6.9	2.7	0.7	0.2	0	0
19th	1.08	1.06	0.58	0.02					0.93	0.18								
18th	1.24	1.28	0.77	0.03					1.18	0.25	0.01							
11th	24.38	28.41	36.95	24.5	5.58				27.72	20.85	15.34	0.01						
10th	■	■	■	■	■	■	■	■	■	■	■	■	■	■	■	■	■	■
3rd				0.01	0.06	0.14	0.3	0.32			0.01	0.1	0.14	0.22	0.29	0.3	0.36	0.35
2nd					0.03	0.09	0.12	0.1			0.01	0.06	0.09	0.11	0.13	0.07	0.16	0.13

Case No.	II1	II2	II3	II4	II5	II6	II7	II8	III1	III2	III3	III4	III5	III6	III7	III8	Ref1	Ref2
Ri	156.9	69.7	39.2	25.1	17.4	9.8	2.5	0.6	42.9	27.5	19.1	10.7	6.9	2.7	0.7	0.2	0	0
19th	23.59	25.1	27.76	23.89	26.7	25.9	20.64	35.21	24.86	21.54	20.58	24.25	23.65	20.19	32.18	41.79	51.42	55.68
18th	■	■	■	■	■	■	■	■	■	■	■	■	■	■	■	■	■	■
11th																		
10th																		
3rd																		
2nd																		

Fig. 15. Color level of reentry ratio in each case (■ source location). (For interpretation of the references to color in this figure legend, the reader is referred to the Web version of this article.)

concentration on the plane at the height of 1.6 m above the floor (human respiration plane), which is near the source height. $M_{i\text{-}j}$ can be directly calculated from the predicted average concentration values of the tracer gas on the two corresponding planes, $M_{i\text{-}j} = C_j/C_i$.

The calculated reentry ratios are shown in Fig. 15. Each column contains the results for a certain case. The six grid boxes along a column represent six concerned rooms in the objective building. The number in each grid box is the reentry ratio value for the corresponding room. The color of the grid box indicates the magnitude of the reentry ratio in this room. A high reentry ratio means a high cross contamination risk. Only the infected units are discussed according to the figure. When the source is located at the windward 2nd floor, the 3rd floor is the most vulnerable. The reentry ratios for the third floor are almost or above 20% when the buoyancy force is stronger (Case II1 - Case II3 and Case III1), and then reduces to near or below 10% when the two forces are approximately equal at lower height (Case II4, CaseIII2 and Case III3). In Case II1, $Ri = 156.9$, the reentry ratios for the middle units, the 10th and 11th floors, are around 1%, and the magnitude for the upper units are 0.1%. When the Ri is 69.7, the reentry ratios for the middle units are in a range of 0.1%–0.2%, and for the upper units are at a magnitude of 0.01%. When the Ri decreases to 42.9, the reentry ratios for the middle units are below 0.1%. In the isothermal cases, the tracer gas cannot go upward.

When the source is released from the 10th floor, the reentry ratios for the 11th floor are over 20% once the Ri numbers exceed 25. As to the lower units, the affected risk exists when the Ri numbers are below 20, and the reentry ratios are generally below 0.5%. In two isothermal cases, the values of R for the bottom two floors are close to ones in the wind effect dominated cases, II7, II8, III7 and III8. For the upper two units, the reentry ratios are around 1% in Case II1 - Case II3 and Case III1 when $Ri > 39$, while it is around 0.2% in Case III2 when $Ri = 27.5$. And the values are below 0.05% in Case II4 and Case III3. Comparison work has been done between the present work and anterior study by Gao [25]. In the previous numerical simulation of cascade effect, the indoor/outdoor temperature difference was 5 K, and the ACH values were both 10.08 in the two concerned rooms under windless condition. The pollutant was generated by a point source in the room with a constant mass flow rate of 8 mg/s. It was found that in a windless day, around 7.5% of the exhaust air from lower unit can re-enter into the upper one, while it's around 25% in the present work. Different mechanisms can be one of the main reasons for the differences on reentry ratio values. In the indoor/outdoor temperature difference driven mode, cold flow enters from the lower part of the window and thermal flow exits from the upper part. The outflow from indoor will not go upward exactly along the wall but have a certain distance with the wall. In the present study, the upward thermal plume is adhering to the wall, so the tracer gas moving with airflow is easier brought into the upper floor, causing a higher reentry ratio. Besides, the source locations and sampling methods of mean concentration may also have influences on the different values of reentry ratio.

When the source location is at the 18th unit, only the 19th floor among the concerned rooms is influenced. The reentry ratios are all over 20%, especially when Ri numbers are below 1, the R values can be up to 30% or even 40%. One thing should be noticed that, for two isothermal cases, both of the reentry ratios exceed 50%, more than twice those of buoyancy lift ruling cases (II1-II3, III1-III2). Compared with the buoyancy force dominant cases, the ACH values in the isothermal cases are much smaller, which means the tracer gas is easier to stay in the source room rather than exhaust to another room. So the specific values $M_{i\text{-}j}$ are lower in the isothermal modes. According to Eq. (13), the reentry ratio is closely related to the concentration ratio and air exchange rate ratio of two units. Take the buoyancy forced Case I1 and isothermal Case Ref1 as the comparison objectives. In Case I1, the concentration ratio between 19th and 18th is about 1/5 while the ACH ratio is almost 1. Thus the reentry ratio is close to 20%. In Case Ref1, the concentration ratio between 19th and 18th is about 1/8 while the ACH ratio is approximate 4. So the reentry ratio is up to 50%. Similarity rules can be found between isothermal cases and combined wind and buoyancy effects forces cases. In general, the upstairs residents should pay more attention to the intervention measures on the control of contamination risk.

4. Conclusions

Concerning the inter-flat pollutant transmission phenomenon, the impact of solar radiation has not been taken into account before. The present work pays attention to this factor, and also the coupling effect of approaching wind and near wall thermal plume originating from solar radiation. The different influences between the sunward surface and shady side surface are compared. Richardson number is adopted to represent the combined effect of buoyancy lift and wind. The pollutant dispersion routes on the windward side under different Ri number cases are analysed. For a 58 m high building at noon of a typical day of transition season in Shanghai, the near wall thermal plume speed at the building height is up to 1.2 m/s. For the pollutant transmission, the source is released from a point at a constant intensity. The following conclusions can be obtained:

(1) In a gentle breezy day, the tracer gas can spread vertically upward driven by thermal flow, from bottom to top in a high-rise building. The reentry ratio of the flat immediately above the source is around 25%. However, for the isothermal condition, the vertically upward transmission is only possible above the stagnation zone, and the reentry ratio can be up to more than 50%. For source location below the stagnation zone conditions, the pollutants disperse from the middle of the building to bottom with the downward flow in the isothermal cases.
(2) As to the comparisons between the sunward and shady side, both of two surfaces are placed at the windward side. Take the gentle breeze cases as contrast objects, the results show that when the source is released from the bottom flat of the building, the vertical upward coverage length of tracer gas on the shady side surface is nearly half of that on the sunward surface. Both of the reentry ratio values of the flat immediately above the source are almost 20%.
(3) In terms of the combined effect of wind and buoyancy forces, multiple cases are set for relevant analysis and investigation. The assigned dimensionless number, Ri, is helpful for summarizing the results. When the source location is above the stagnation zone, the pollutant always goes up with the rising airflow. Under the conditions of the source location below the stagnation zone, as the Ri number decreases, the effect of force convection strengthens, so the pollutant spread from lower floor to upper ones is weakened. As the source located at the 2nd floor, the vertical upgrade transmission is suppressed once Ri is lower than 40. When the source is released from the 10th floor, the vertical upward transmission is restrained once Ri is smaller than 20.

Overall, the vertical upward transmission driven by wall thermal plume and the affected risks of leeward units from a windward source should not be overlooked in a high-rise building. There are still many limitations in the present study. The airflow patterns around an isolated building under different meteorological conditions are diverse. The direction of approaching wind has been proved as one of the main influencing factors, which is not considered in this paper. Besides, the near wall flow features are distinct in daylight and night, also in different seasons. In addition, the calculations in this paper are based on steady-state simulations without considering the effect of time-dependent dynamics on heat and mass transfer. The selection of more applicable dimensionless numbers can be another issue, since a global Ri number has limitations to reflect a local pollutant dispersion phenomenon for a large scale problem, such as in the high-rise building. Further investigations are worthy to be done on the above matters.

Acknowledgements

This research is funded by the Natural Science Foundation of China (No.51278348) and the Fundamental Research Funds for the Central Universities of China.

References

[1] J.W. Tang, Y. Li, I. Eames, et al., Factors involved in the aerosol transmission of infection and control of ventilation in healthcare premises, J. Hosp. Infect. 64 (2) (2006) 100–114.
[2] J. Barker, D. Stevens, S.F. Bloomfield, Spread and prevention of some common viral infections in community facilities and domestic homes, J. Appl. Microbiol. 91 (1) (2010) 7–21.
[3] M.J. Mendell, W.J. Fisk, K. Kreiss, et al., Improving the health of workers in indoor environments: priority research needs for a national occupational research agenda, Am. J. Publ. Health 92 (9) (2002) 1430–1440.
[4] M. Nicas, W.W. Nazaroff, A. Hubbard, Toward understanding the risk of secondary airborne infection: emission of respirable pathogens, J. Occup. Environ. Hyg. 2 (3) (2005) 143–154.
[5] R. Tellier, Review of aerosol transmission of influenza A virus, Emerg. Infect. Dis. 12 (11) (2006) 1657–1662.
[6] Q. Chen, Ventilation performance prediction for buildings: a method overview and recent applications, Build. Environ. 44 (4) (2009) 848–858.
[7] Q. Xia, J. Niu, X. Liu, Dispersion of air pollutants around buildings: a review of past studies and their methodologies, Indoor Built Environ. 23 (2) (2014) 201–224.
[8] R.E. Britter, S.R. Hanna, Flow and dispersion in urban areas, Annu. Rev. Fluid Mech. 35 (1) (2003) 469–496.
[9] H.C. Cheung, W. Tao, K. Baumann, et al., Influence of regional pollution outflow on the concentrations of fine particulate matter and visibility in the coastal area of southern China, Atmos. Environ. 39 (34) (2005) 6463–6474.
[10] D. Massey, J. Masih, A. Kulshrestha, et al., Indoor/outdoor relationship of fine particles less than 2.5 μm (PM2.5) in residential homes locations in central Indian region, Build. Environ. 44 (10) (2009) 2037–2045.
[11] L. Zhao, C. Chen, P. Wang, et al., Influence of atmospheric fine particulate matter (PM 2.5) pollution on indoor environment during winter in Beijing, Build. Environ. 87 (2015) 283–291.
[12] K. Schenkel, R. Amarosa, I. Mücke, Risk Assessment Guidelines for Infectious Diseases Transmitted on Aircraft, Europe Centre for Disease Prevention and Control, 2009, pp. 1–58.
[13] H. Qian, Y. Li, P.V. Nielsen, et al., Dispersion of exhaled droplet nuclei in a two-bed hospital ward with three different ventilation systems, Indoor Air 16 (2) (2010) 111–128.
[14] Y. Li, G.M. Leung, J.W. Tang, et al., Role of ventilation in airborne transmission of infectious agents in the built environment – a multidisciplinary systematic review, Indoor Air 17 (1) (2007) 2–18.
[15] I. Mavroidis, R.F. Griffiths, D.J. Hall, Field and wind tunnel investigations of plume dispersion around single surface obstacles, Atmos. Environ. 37 (21) (2003) 2903–2918.
[16] I.T. Yu, Evidence of airborne transmission of the severe acute respiratory syndrome virus, N. Engl. J. Med. 350 (17) (2004) 1731–1739.
[17] Y. Li, X. Huang, I.T. Yu, et al., Role of air distribution in SARS transmission during the largest nosocomial outbreak in Hong Kong, Indoor Air 15 (2) (2010) 83–95.
[18] Y. Li, S. Duan, I.T.S. Yu, et al., Multi-zone modeling of probable SARS virus transmission by airflow between flats in Block E, Amoy Gardens, Indoor Air 15 (2) (2005) 96–111.
[19] Y. Li, W.H. Ching, H. Qian, et al., An evaluation of the ventilation performance of new SARS isolation wards in nine Hospitals in Hong Kong, Indoor Built Environ. 16 (5) (2007) 400–410.
[20] H. Humphreys, Positive-pressure isolation and the prevention of invasive aspergillosis. What is the evidence? J. Hosp. Infect. 56 (2) (2004) 93–100.
[21] B. Zhao, J. Wu, Numerical investigation of particle diffusion in a clean Room, Indoor Built Environ. 14 (6) (2005) 469–479.
[22] N.P. Gao, J.L. Niu, M. Perino, et al., The airborne transmission of infection between flats in high-rise residential buildings: particle simulation, Build. Environ. 44 (2) (2009) 402–410.
[23] J.L. Niu, T.C.W. Tung, On-site quantification of re-entry ratio of ventilation exhausts in multi-family residential buildings and implications, Indoor Air 18 (1) (2008) 12–26.
[24] X.P. Liu, J.L. Niu, M. Perino, et al., Numerical simulation of inter-flat air cross-contamination under the condition of single-sided natural ventilation, J. Build. Perform. Simulat. 1 (2) (2008) 133–147.
[25] N.P. Gao, J.L. Niu, M. Perino, et al., The airborne transmission of infection between flats in high-rise residential buildings: tracer gas simulation, Build. Environ. 43 (11) (2008) 1805–1817.
[26] X.P. Liu, J.L. Niu, K.C.S. Kwok, et al., Investigation of indoor air pollutant dispersion and cross-contamination around a typical high-rise residential building: wind tunnel tests, Build. Environ. 45 (8) (2010) 1769–1778.
[27] X.P. Liu, J.L. Niu, K.C.S. Kwok, et al., Local characteristics of cross-unit contamination around high-rise building due to wind effect: mean concentration and infection risk assessment, J. Hazard Mater. 192 (1) (2011) 160–167.
[28] X.P. Liu, J.L. Niu, K.C. Kwok, Analysis of concentration fluctuations in gas dispersion around high-rise building for different incident wind directions, J. Hazard Mater. 192 (3) (2011) 1623–1632.
[29] D. Mu, N.P. Gao, T. Zhu, Wind tunnel tests of inter-flat pollutant transmission characteristics in a rectangular multi-storey residential building, part A: effect of wind direction, Build. Environ. 108 (2016) 159–170.
[30] D. Mu, C. Shu, N.P. Gao, et al., Wind tunnel tests of inter-flat pollutant transmission characteristics in a rectangular multi-storey residential building, part B: effect of source location, Build. Environ. 114 (2017) 281–292.
[31] Z.T. Ai, C.M. Mak, J.L. Niu, Numerical investigation of wind-induced airflow and interunit dispersion characteristics in multi-storey residential buildings, Indoor Air 23 (5) (2013) 417–429.
[32] Z.T. Ai, C.M. Mak, A study of inter-unit dispersion around multi-storey buildings with single-sided ventilation under different wind directions, Atmos. Environ. 88 (5) (2014) 1–13.
[33] Z.T. Ai, C.M. Mak, Large eddy simulation of wind-induced inter-unit dispersion around multi-storey buildings, Indoor Air 26 (2) (2016) 259–273.
[34] J. Mao, N. Gao, The airborne transmission of infection between flats in high-rise residential buildings: a review, Build. Environ. 94 (3) (2015) 516–531.
[35] Y. Tominaga, T. Stathopoulos, Numerical simulation of dispersion around an isolated cubic building: model evaluation of RANS and LES, Build. Environ. 45 (10) (2010) 2231–2239.
[36] Y. Tominaga, T. Stathopoulos, Ten questions concerning modeling of near-field pollutant dispersion in the built environment, Build. Environ. 105 (2016) 390–402.
[37] R. Ooka, T. Sato, K. Harayama, et al., Thermal energy balance analysis of the Tokyo metropolitan area using a mesoscale meteorological model incorporating an urban canopy model, Boundary-Layer Meteorol. 138 (1) (2011) 77–97.
[38] Y. Fan, Y. Li, J. Hang, et al., Natural convection flows along a 16-storey high-rise building, Build. Environ. 107 (2016) 215–225.
[39] C. Georgakis, M. Santamouris, Experimental investigation of air flow and temperature distribution in deep urban canyons for natural ventilation purposes, Energy Build. 38 (4) (2006) 367–376.
[40] X. Xie, Z. Huang, J. Wang, et al., The impact of solar radiation and street layout on pollutant dispersion in street canyon, Build. Environ. 40 (2) (2005) 201–212.
[41] K. Richards, M. Schatzmann, B. Leitl, Wind tunnel experiments modelling the thermal effects within the vicinity of a single block building with leeward wall heating, J. Wind Eng. Ind. Aerod. 94 (8) (2006) 621–636.
[42] T.S. Larsen, P. Heiselberg, Single-sided natural ventilation driven by wind pressure and temperature difference, Energy Build. 40 (6) (2008) 1031–1040.
[43] M.Z.I. Bangalee, J.J. Miau, S.Y. Lin, et al., Flow visualization, PIV measurement and CFD calculation for fluid-driven natural cross-ventilation in a scale model, Energy Build. 66 (6) (2013) 306–314.
[44] A. Dama, D. Angeli, Wind and buoyancy driven natural ventilation in double skin facades, Int. J. Vent. 15 (3–4) (2016) 288–301.
[45] ASHRAE, ASHRAE Handbook, American Society of Heating, Refrigerating, and Air-Conditioning Engineers. HVAC Applications, Atlanta, GA, 2015 section 45.3.
[46] Q. Yan, Q. Zhao, Building Thermal Process, China Architecture and Building Press, 1986 (Chapter 2).
[47] B. Wang, G. Pan, The state of atmospheric transparency over China, Acta Meteorol. Sin. 40 (4) (1982) 443–452.
[48] J. Han, Analysis on the characteristics of atmospheric transparency in Shanghai, Annual meeting of the China Meteorological Society, 2011, pp. 1–9.
[49] M. Wang, X. Sun, Analysis on atmospheric transparency and direct solar radiation at noon, Sol. Energy 12 (2015) 32–36.
[50] Y.Q. Lu, Practical Design Manual for Heating and Air Conditioning, second ed., China Architecture and Building Press, 2008 (Chapter 4).
[51] ASHRAE Task group, Procedure for Determining Heating and Cooling Loads for Computerizing Energy Calculations, Algorithms for building heat transfer subroutines ASHRAE, New York, 1975, pp. 76–78.
[52] J.A. Palyvos, A survey of wind convection coefficient correlations for building envelope energy systems' modeling, Appl. Therm. Eng. 28 (8) (2008) 801–808.
[53] N. Ito, K. Kimura, J. Oka, Field experiment study on the convective heat transfer coefficient on exterior surface of a building, Build. Eng. 78 (1) (1972) 184–191.
[54] A. Madhlopa, C. Johnstone, Numerical study of a passive solar still with separate condenser, Renew. Energy 34 (7) (2009) 1668–1677.
[55] X.B. Wang, C. Huang, L.H. Wang, Experimental study of temperature distribution and heat transfer coefficient of vertical exterior surface of a building, Fluid Mach. 39 (1) (2011) 69–73.
[56] J. Franke, A. Hellsten, H. Schlünzen, B. Carissino, Best Practice Guideline for the CFD Simulation of Flows in the Urban Environment, COST Office, Brussels, 2007.
[57] P. Roache, J. Perspective: a method for uniform reporting of grid refinement studies, J. Fluid Eng. 116 (3) (1994) 405–413.
[58] ASHRAE, ASHRAE Handbook, American Society of Heating, Refrigerating and Air-conditioning Engineers. Fundamentals (SI), Atlanta, GA, 2009 section 10.4.
[59] W.Q. Tao, Numerical Heat Transfer, second ed., Xi'an Jiaotong University Press, 2011 (Chapter 9).
[60] V. Yakhot, S.A. Orszag, S. Thangam, et al., Development of turbulence models for shear flows by a double expansion technique, Phys. Fluid. 4 (7) (1992) 1510–1520.
[61] P.L. Betts, I.H. Bokhari, Experiments on turbulent natural convection in an enclosed tall cavity, Int. J. Heat Fluid Flow 21 (6) (2000) 675–683.
[62] Y. Jiang, D. Alexander, H. Jenkins, Natural ventilation in buildings: measurement in a wind tunnel and numerical simulation with large-eddy simulation, J. Wind Eng. Ind. Aerod. 91 (3) (2003) 331–353.